

Model of Bipolar Electrogram Fractionation and Conduction Block Associated with Activation Wavefront Direction at Infarct Border Zone Lateral Isthmus Boundaries

Edward J. Ciaccio, Hiroshi Ashikaga, James Coromilas, Bruce Hopenfeld, Daniel Cervantes, Andrew L. Wit, Nicholas S. Peters, Elliot R. McVeigh and Hasan Garan

Circ Arrhythm Electrophysiol. published online January 19, 2014;

Circulation: Arrhythmia and Electrophysiology is published by the American Heart Association, 7272 Greenville Avenue, Dallas, TX 75231

Copyright © 2014 American Heart Association, Inc. All rights reserved.

Print ISSN: 1941-3149. Online ISSN: 1941-3084

The online version of this article, along with updated information and services, is located on the World Wide Web at:

<http://circep.ahajournals.org/content/early/2014/01/19/CIRCEP.113.000840>

Permissions: Requests for permissions to reproduce figures, tables, or portions of articles originally published in *Circulation: Arrhythmia and Electrophysiology* can be obtained via RightsLink, a service of the Copyright Clearance Center, not the Editorial Office. Once the online version of the published article for which permission is being requested is located, click Request Permissions in the middle column of the Web page under Services. Further information about this process is available in the [Permissions and Rights Question and Answer](#) document.

Reprints: Information about reprints can be found online at:
<http://www.lww.com/reprints>

Subscriptions: Information about subscribing to *Circulation: Arrhythmia and Electrophysiology* is online at:
<http://circep.ahajournals.org/subscriptions/>

**Model of Bipolar Electrogram Fractionation and Conduction Block
Associated with Activation Wavefront Direction at Infarct Border Zone
Lateral Isthmus Boundaries**

Running title: *Ciaccio et al.; Model of Bipolar Electrogram Fractionation*

Edward J. Ciaccio, PhD¹; Hiroshi Ashikaga, MD, PhD^{2,3}; James Coromilas, MD⁴;

Bruce Hopenfeld, PhD³; Daniel Cervantes, MD⁵; Andrew L. Wit, PhD⁵;

Nicholas S. Peters, MD, PhD⁶; Elliot R. McVeigh, PhD³; Hasan Garan, MD¹

¹Department of Medicine, Division of Cardiology, ⁵Department of Pharmacology, Columbia University Medical Center, New York, NY; ²Division of Cardiology, ³Department of Biomedical Engineering, Johns Hopkins University, Baltimore, MD; ⁴Department of Medicine, Division of Cardiology, University of Medicine and Dentistry of New Jersey, New Brunswick, NJ; ⁶Department of Medicine, Division of Cardiology, Imperial College, London, United Kingdom

JOURNAL OF THE AMERICAN HEART ASSOCIATION

Correspondence:

Edward J. Ciaccio, PhD

Presbyterian Hospital 7W-318

630 West 168th Street

Columbia University

New York NY 10032

Tel: 212-305-5447

Fax: 212-342-0447

E-mail: ciaccio@columbia.edu

Journal Subject Codes: [5] Arrhythmias, clinical electrophysiology, drugs, [106] Electrophysiology, [130] Animal models of human disease, [132] Arrhythmias - basic studies, [157] Quantitative modeling

Abstract:

Background - Improved understanding of the mechanisms underlying infarct border zone (IBZ) electrogram fractionation may be helpful to identify arrhythmogenic regions in the post-infarction heart. We describe the generation of electrogram fractionation from changes in activation wavefront curvature in experimental canine infarction.

Methods and Results - A model was developed to estimate the extracellular signal shape that would be generated by wavefront propagation parallel to versus perpendicular to the lateral boundary (LB) of the reentrant ventricular tachycardia (VT) isthmus, or diastolic pathway. LBs are defined as locations where functional block forms during VT, and elsewhere they have been shown to coincide with sharp thin-to-thick transitions in IBZ thickness. To test the model, bipolar electrograms were acquired from IBZ sites in 10 canine heart experiments 3-5 days after experimental infarction. Activation maps were constructed during sinus rhythm and during VT. The characteristics of model-generated versus actual electrograms were compared. Quantitatively expressed VT fractionation (7.6 ± 1.2 deflections, 16.3 ± 8.9 ms intervals) was similar to model-generated values with wavefront propagation perpendicular to the LB (9.4 ± 2.4 deflections, 14.4 ± 5.2 ms intervals). Fractionation during sinus rhythm (5.9 ± 1.8 deflections, 9.2 ± 4.4 ms intervals) was similar to model-generated fractionation with wavefront propagation parallel to the LB (6.7 ± 3.1 deflections, 7.1 ± 3.8 ms intervals). VT and sinus rhythm fractionation sites were adjacent to LBs approximately 80% of the time.

Conclusions - The results suggest that in a subacute canine infarct model, the LBs are a source of activation wavefront discontinuity and electrogram fractionation, with the degree of fractionation being dependent upon activation rate and wavefront orientation with respect to the LB.

Keywords: cardiac electrophysiology, left ventricle geometry, modeling, ventricular, wavebreak, curvature, electrogram, fractionation, functional block, wavefront

Background

Ventricular tachycardia (VT) caused by a reentrant circuit is a life-threatening arrhythmia following myocardial infarction¹. Canine and swine models of experimental infarction can be useful to study the electrophysiologic characteristics of this arrhythmia²⁻⁴. In a canine infarction model, the VT reentrant circuit often resides in the infarct border zone (IBZ), which is the thin region of surviving myocardium between the infarct rim and the epicardial surface^{2,5,6}. For the canine infarction model, the IBZ is thinnest at the reentrant circuit isthmus location^{2,5,6}. Away from the isthmus, IBZ thickness increases sharply, and it has been shown previously that points of sharpest thin-to-thick IBZ transition coincide with locations where functional block is present during reentrant VT. These locations where functional block forms during VT are defined as lateral isthmus boundaries (LB). The LBs are distinctive from the isthmus entrance and exit, through which the activation wavefront propagates during VT.

In previous work we described a geometry-to-propagation model in subacute canine infarction which was based upon IBZ geometric relationships². The IBZ thickness was measured by magnetic resonance imaging (MRI)⁷ and histology⁶. It was predicted that at sharp thin-to-thick transition sites, which occurred along the LBs, curvature of the outward-directed propagating activation wavefront would be convex (i.e., curved outward so that the conducting volume being electrically activated would be greater than the volume previously activated). At the LBs, wavefront convexity can attain a critical degree of curvature so that there is difficulty in providing sufficient electrical charge to the larger volume of tissue distal to the activating wavefront, resulting in very slow electrical conduction or functional block. It was also predicted that propagation across isthmus edges would be possible at segments of the boundary with more gradual thickness transition, and that these segments would serve as isthmus entrance and exits

points for the activation wavefront during reentrant VT. These predictions were compared with actual functional lines of block and entrance and exit point locations in reentrant circuits, as determined by a dense array of activation mapping during VT, with good agreement.

Fractionation can be defined as broad-based electrograms with multiple deflections that continue for at least 50ms in duration; it is often associated with the isthmus of the reentrant circuit or with scar^{8,9,10}. Establishing the precise relationship between fractionation and the isthmus region at the center of reentry, therefore, could be helpful for targeting arrhythmogenic regions during ablative therapy. Although prior work has described some of the underlying electrophysiological causes for fractionated electrograms^{11,12} their relationship to IBZ geometry and the resulting changes in wavefront curvature and conduction velocity has not been elucidated. In this study we propose a model to explain the genesis of local electrogram fractionation, based upon variable thin-to-thick transition at the LB. To test our model, bipolar electrograms were acquired from the epicardial IBZ in subacute infarction canine heart experiments, and the actual degree of fractionation was compared with the predictions of our model.

Method

Canine Data Acquisition and Analysis

In 10 purpose-bred canines weighing 20–40 kg, while anesthetized with sodium pentobarbital (30 mg/kg intravenously), the left anterior descending coronary artery (LAD) was ligated near its base¹³. This resulted in a transmural anteroseptal myocardial infarction with survival of an epicardial rim of muscle having variable thickness, which we have designated as the epicardial border zone, and referred to here as the IBZ. The animals were prepared for electrophysiologic study 3-5 days after LAD ligation, the interval when the post-infarction canine heart is most

likely to be arrhythmogenic^{5,6,11,12}. Programmed electrical stimulation through bipolar electrodes sutured on the left ventricle, both adjacent to and within the IBZ, was used to induce VT. Bipolar electrograms were recorded simultaneously from 196-312 sites. All electrophysiological methods have been previously described in detail¹³. All canine experiments were done with the approval of the Institutional Review Board of Columbia University Medical Center. The procedures followed during the experiments were in accord with institutional guidelines.

The data acquisition system consisted of a multichannel bipolar electrode array that provided analog signal inputs that were first bandpass filtered and then digitized at 1-2 kHz per channel. Further system details are described elsewhere¹⁴, and mathematical details for registration of the multielectrode array with respect to IBZ landmarks have also been described¹⁵. Local bipolar electrograms were recorded from the epicardial surface of the IBZ, and electrical activation maps were constructed from electrograms recorded during sinus rhythm and during VT. The activation maps were constructed by converting the activation times during one cardiac cycle to colors from red (early) to blue (late) on a computerized grid, and automatically drawing isochrones with a spacing of approximately 20 milliseconds between them. On these maps, block lines were then drawn manually based upon two criteria. A line of block was identified whenever the activation on either side of the line was disparate by greater than 40 milliseconds, and the wavefront traveled in different directions on either side of the line. No block lines were present in any of the sinus rhythm activation maps. Thus block lines evident in VT maps were likely to be functional, not structural. From the reentrant VT activation maps, the border of the reentrant circuit isthmus was defined as the location of bounding functional lines of block that were connected by straight lines at their ends¹⁶. Following reproducible induction and termination of VT, when possible in the 10 postinfarction canine experiments, ventricular pacing (V-Pace) was

performed from the isthmus region at the same cycle length as VT during normal sinus rhythm. These recordings were also marked and mapped for activation time and used for further analysis.

Fractionation Model Equations

Alterations in the geometry of the conducting medium result in wavefront curvature changes, which can cause slow conduction and block in isolated cardiac muscle¹⁷. A change from smaller to larger volume in the direction of electrical wavefront propagation results in a change from high to low impedance, with the current flow at the transition being insufficient to depolarize the distal, thicker segment of tissue. Based on this phenomenon, it can be shown that conduction velocity in the IBZ, symbolized as theta (θ), can be approximated as²:

$$\theta \approx \theta_0 \pm \frac{D}{c} \cdot \frac{\Delta T}{T} \quad (1)$$

where θ_0 is the conduction velocity when there is no curvature along the leading edge of the activation wavefront (i.e., when the wavefront is rectilinear), D is the diffusion coefficient, which is the current flow due to the cell membrane voltage gradient (0.05 – 0.2mm²/ms in ventricular myocardium¹⁸), c is the spatial resolution, or space step, in units of millimeters, T is IBZ thickness, where the thickness direction, perpendicular to the epicardial surface, is defined to be the Z-axis, and ΔT is the IBZ thickness change over one space step as the leading edge of the wavefront propagates in the XY plane. When the thickness transition is thin-to-thick, the wavefront leading edge becomes convex, i.e., it is curved outward so that the conducting volume being activated is greater than the volume previously activated, and the sign in Eq. 1 is negative, resulting in wavefront slowing. Conversely, when the thickness transition is thick-to-thin, the wavefront leading edge becomes concave, i.e., curved inward so that the conducting volume being activated is less than the volume previously activated, which results in wavefront acceleration, symbolized by a positive sign in Eq. 1.

The influence of thin-to-thick versus thick-to-thin wavefront propagation on the conduction velocity will differ, even when the absolute magnitude of the last term in Eq. 1 is identical. Suppose that $\theta_0 = 0.4$ mm/ms in the IBZ, and let the diffusion coefficient $D = 0.1$ mm²/ms, and the spatial resolution $c = 1$ mm. Thus $D / c = 0.1$ mm/ms and is a constant. Furthermore, suppose the isthmus region is ~ 100 μ m in thickness and at the immediately adjacent outer circuit pathway the thickness is ~ 500 μ m, in accord with prior observations^{2,5,6}. Then $\Delta T / T = 400/100 = 4$, and the magnitude of the term on the right-hand-side in Eq. 1 is 0.4. In the thin-to-thick direction, this is the critical degree of curvature resulting in a conduction velocity $\theta = 0.4 - (0.1 \times 4) = 0$ mm/ms, i.e., there is conduction block. Values of $\Delta T / T > 4$ also lead to conduction block, while values of $\Delta T / T < \sim 4$ will result in slowed conduction. In Figure 1 are shown graphs of the relationship when the absolute value of the right-hand-term is $< \sim 0.4$. The time to traverse a 1 millimeter distance when $\theta = 0.4$ mm/ms, which occurs when the right-hand-side in Eq. 1 is zero, is 2.5 milliseconds (left-most point in each graph). When the right-hand term in Eq. 1 has a value of -0.39, so that $\theta = 0.4 - 0.39 = 0.01$ mm/ms, the time to traverse the 1 millimeter distance is approximately 100 milliseconds – there is a substantial slowing of the wavefront (panel A). As the right-hand term in Eq. 1 approaches a value of 0.4 mm/ms, the conduction velocity will approach zero, i.e., conduction block can occur. Anywhere along the region with steep slope in panel A, when there is even a small change in $\Delta T/T$, it will result in a large change in the time to conduct the wavefront. Conversely, when the right-hand term in Eq. 1 has a value of +0.39, so that $\theta = 0.4 + 0.39 = 0.79$ mm/ms, the time to traverse the 1 millimeter distance shortens from 2.5 milliseconds to approximately $1 \text{ mm} / 0.79 \text{ mm/ms} = 1.3$ milliseconds (right-hand side in panel B). Therefore, as also can be seen in panel C by superimposing the traces of panels A and B, large absolute changes in conduction time occur not when $D/c \cdot \Delta T/T$

$\rightarrow +\theta_0$, but only when $D/c \cdot \Delta T/T \rightarrow -\theta_0$, which is along the portion of the trace in panel C noted by an asterisk (*). Supposing that D/c is a constant, this portion of the curve will be realized when T is small and ΔT is large, i.e. when wavefront propagation is in the outward direction at the edge of the thinnest portion of the border zone, where it transitions to sharply thicker border zone, which occurs at the LBs.

Based upon the traces of Figure 1, it can be demonstrated that the geometry of the IBZ conducting medium influences functional block line formation during reentrant VT². This is shown in schematized form in Figure 2A. The IBZ is the region between infarct (green) and epicardial surface, and XYZ coordinate axes are noted. The IBZ is thinnest above the rectangular portion of the infarct at center, noted at one location by the short vertical dashed line. Entrance and exit points are ramps of gradual IBZ thickness change, and their ends are denoted by longer vertical dashed lines. The wavefront enters the isthmus region along the left-hand ramp where there is a gradual transition from thick-to-thin IBZ. The wavefront, shown in red, is concave along the Z-axis during the transition, which facilitates more rapid inward wavefront propagation toward the isthmus (right-hand term in Eq. 1 is positive). As the wavefront travels through the isthmus region during VT where there is no change in IBZ thickness, it becomes rectilinear (flat). It is blocked from moving laterally by the sharp thin-to-thick transitions across the LBs. However at the downward ramp, the more gradual transition prevents wavefront curvature from becoming critically convex so that propagation proceeds, although slowing occurs (right-hand term in Eq. 1 is negative but with magnitude less than θ_0). The wavefront then bifurcates, travels along the outer pathway of the reentrant circuit as two distinct wavefronts, and then coalesces at the isthmus entrance, forming double-loop reentry.

Figure 2B shows how conduction velocity can change when there is variable steepness

along the LBs. Colors from red to blue denote early-to-late activation time during one VT cycle. The more gradual thickness transition at the LBs as compared with panel A enables very slow and variable propagation outward from them (denoted as short arrows on one side). At points along the LB with a more gradual slope, the convex, outwardly propagating wavefront will travel more rapidly since ΔT in Eq. 1 will be of lesser magnitude. At points along the LB with a sharper slope, the wavefront will travel more slowly since ΔT in Eq. 1 will be of greater magnitude. Depending upon the variability in thickness transition along the LB, and the resulting dramatic differences in slow conduction velocity according to the region of the trace with asterisk in Figure 1C, discontinuity in the wavefront propagation can occur, leading to the possibility of electrogram fractionation. Individual wavefronts along faster edges of the LB will not propagate and merge into the pathways of slower portions of the wavefront, because of the sharp thin-to-thick transition between them (Figure 2B).

During normal sinus rhythm, propagation in the same direction across the LB would be expected to result in wavefront discontinuity, although to a lesser extent due to the longer cardiac cycle¹⁹. Propagation in the opposite direction, from thick-to-thin, would not result in wavefront discontinuity, according to the trace of Figure 1B, since only small changes in increased conduction velocity would occur. If the activation wavefront propagates in parallel to the LBs during sinus rhythm, wavefront discontinuity and the possibility of electrogram fractionation can occur as illustrated in Figure 2C. The wavefront blocks at points of sharp thin-to-thick transition along the LB edges, as denoted by vertical straight lines. At these points, the wavefront becomes discontinuous and must travel around, as shown by curved arrows. The propagating wavefront would not be expected to become highly discontinuous, however, since there is no impediment to propagation along the centerline.

To estimate electrogram fractionation based upon the geometric changes in the conducting medium, the extracellular voltage ϕ_e caused by activation wavefront propagation can be described using the following equation, as illustrated in Figure 3A²⁰:

$$\phi_e(P, t_o) = \left(\frac{1}{4\pi\sigma_e}\right) \sum_j \frac{\left[\frac{\partial}{\partial x} (\sigma_{ix} \frac{\partial \phi_i}{\partial x}) + \frac{\partial}{\partial y} (\sigma_{iy} \frac{\partial \phi_i}{\partial y}) \right]}{[(a+b)^2 + d^2]^{1/2}} (2a \cdot dx \cdot dy) \quad (2)$$

where P is the observation point at time t_o , the intracellular voltage is ϕ_i , the intracellular and extracellular conductivity are σ_i and σ_e , respectively, $\partial \phi_i / \partial x$ and $\partial \phi_i / \partial y$ are proportional to the transmembrane current per unit volume I_m , and ∂ denotes the partial differential. Regarding dimensions, 'a' is the distance from the epicardial surface to the midpoint of the IBZ along the Z-axis (thickness) direction, 'b' is the distance between the point of observation and the epicardial surface, 'd' is the distance in the XY plane from the source of activation to the observation point, dx and dy are unit distances equal to the spatial resolution of the grid, and activation wavefront propagation is in the XY coordinate plane. In Eq. 2, the summation is taken for all grid squares j and the denominator is the distance r between the observation point $\phi_e(P, t_o)$ and a point on the wavefront leading edge:

$$r = \sqrt{(a+b)^2 + d^2} \quad (3)$$

As a first approximation, suppose that the change in intracellular potential, and the intracellular conductivity, are uniform throughout the IBZ, and that the recording electrode is at the heart surface so that $b = 0$. Eq. 2 can then be approximated as:

$$\phi_e(P, t_o) \approx \sum_j \frac{k1}{[a + d^2]^{1/2}} \quad (4)$$

where k1 is a constant, the summation is over all grid points j that are activating at time t_o

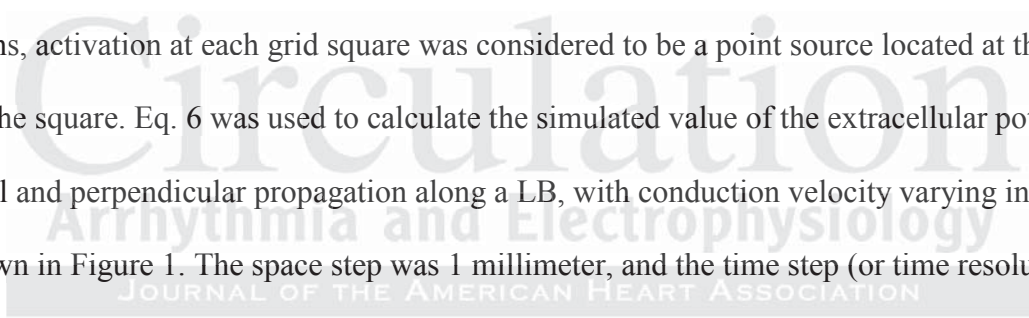
(denoted as unit squares of dimension $dx \ dy$ in Figure 3A) and:

$$d = \sqrt{x^2 + y^2} \quad (5)$$

with x and y being the distances from source to recording electrode along the X and Y axes. To further simplify the equation, suppose $a \ll d$ (that is, half the IBZ thickness at the observation point is much less than the distance from activation to observation point), and let 'k2' be a constant that prevents the denominator from approaching zero, then:

$$\phi_e(P, t_o) = \sum_j \frac{k1}{k2 + \sqrt{x_j^2 + y_j^2}} \quad (6)$$

with the summation, as in Eq. 4, being over all grid squares j that are activating at time t_o . For calculations, activation at each grid square was considered to be a point source located at the center of the square. Eq. 6 was used to calculate the simulated value of the extracellular potential for parallel and perpendicular propagation along a LB, with conduction velocity varying in the range shown in Figure 1. The space step was 1 millimeter, and the time step (or time resolution, equivalent to digital sampling rate) was 1 millisecond, consistent with actual sampling rates used in clinical recording systems. The activation wavefront was presumed to propagate in only one direction: from thin-to-thick in the direction perpendicular to the LB in one simulation, and in parallel with the LB for the other simulation. The bipolar electrode was oriented as adjacent diagonally oriented grid squares with respect to the LB, which would be the average orientation by random chance. Each electrode was considered to be a point located at the center of each grid square, so that interelectrode distance between the bipoles, based upon the Pythagorean theorem, was $\sqrt{1+1} = 1.414$ millimeters. Ten distinct sharp transitions with randomly changing slope, separated by 1 millimeter distances along the LB, were used for simulation (examples of eight transitions are schematized in Figure 2B). The magnitude of each transition was a random value



ranging from 100 μ m to 490 μ m in thickness over a 1mm distance (maximum $\Delta T/T = 3.9$, corresponding to a minimum conduction velocity = 0.01 mm / ms), which is in accord with prior observations^{2,5,6}. Ten point sources were used, one at each of the 10 sharp transitions, so that the summation in Eq. 6 was over 10 values. The configuration is shown in Figure 3B. The wavefront leading edge, consisting of 10 discrete points, is discontinuous after passage across thin-to-thick IBZ transitions. The wavefront propagates toward and across the diagonally oriented bipolar electrode.

Since the bipolar extracellular signal was calculated, Eq. 6 was implemented as follows:

$$\phi_e(B,t) = \sum_j \left[\frac{k1}{k2 + \sqrt{x_{j,p}^2 + y_{j,p}^2}} - \frac{k1}{k2 + \sqrt{x_{j,n}^2 + y_{j,n}^2}} \right] \quad (7)$$

where p and n represent the positive and negative electrode, respectively, j is one of ten discontinuous points on the leading edge of the wavefront that are activating at time t, and $\phi_e(B,t)$, the bipolar extracellular potential, is calculated for all time t = 1 to 175 milliseconds in 1 millisecond steps to form the electrogram. The electrogram amplitude ϕ_e was normalized by scaling k1 so that a biphasic electrogram deflection would exhibit a 2 mV peak-to-peak amplitude when acquired from a bipolar electrode oriented diagonal to a uniformly propagating wavefront.

Measurements used to Test the Model

The degree of overlap of the arcs of conduction block forming during VT versus V-Pace was determined by overlapping activation maps on the computerized grid. Portions of the two block lines were considered overlapped if they were located between the same recording sites and had the same orientation. The percent of the total VT block line length that was overlapped by V-Pace block lines was tabulated.

The number of fractionated electrogram sites immediately adjacent to VT block line locations (within one recording site), versus those without such an association, was tabulated. The number of sinus rhythm versus VT and V-Pace fractionation sites that coincided was determined (whether or not they were adjacent to a block line location). The characteristics of fractionated electrograms were tabulated over a 175ms interval in terms of the number of deflections, the deflection duration, and number of zero-crossings across a spline interpolation average with 100ms intervals between interpolation points. The analysis interval was selected as 175ms since this is approximately the average VT cycle length in the canine model. These measurements were made using 20 recordings each for VT, V-Pacing, and sinus rhythm. The 20 recordings were comprised of two electrograms from each of the 10 experiments. The pair of recording sites analyzed from each experiment were spatially distinct and selected at random. The same measurements were made for 20 model-generated electrograms (parallel and perpendicular to the LB). Although fractionated electrograms have low amplitude peaks, the tallest of these peaks in each fractionation sequence was used as a reference for detection of distinct electrogram deflections. For each fractionated electrogram (actual or model-generated), deflections were counted as distinct if the positive or negative -going peak of the deflection extended to at least 20% of the absolute height of the tallest deflection, with height being referenced to the local spline interpolation average level.

All electrogram data was normally distributed and expressed as mean \pm standard deviation. To a first approximation, each electrogram was considered to be a random vector uncorrelated to other electrograms. This approximation was previously shown to be satisfactory in the sense that the correlation matrix is sparse, using the same type of bipolar canine postinfarction data as was acquired in the current study²¹. Statistical comparisons were therefore

made between mean electrogram parameters using the unpaired t-test (SigmaPlot Ver. 9, 2004). Correction were done using the Bonferroni method for comparisons of five measurements having different parameters and data type, so that the significance level was taken as $p < 0.05 / 5$, i.e., $p < 0.01$. To check for electrogram correlation between recording sites, the standard deviation in electrogram morphology over 10 sites in a single experiment was compared with the standard deviation in the data pooled from all experiments. Similar values in standard deviation would suggest a similar lack of correlation in electrogram morphology between sites in a single experiment with respect to the lack of correlation when comparing electrograms from different experiments. The F-test was used for comparisons (MedCalc ver. 11.6, 2011, MedCalc Software bvba, Ostend, Belgium).

Results

Examples of actual fractionated electrograms acquired from the LBs during monomorphic VT are provided in Figure 4A. Continuous electrogram deflections without an isoelectric interval extend for much of the 175ms duration of each trace. The signal peaks tend to be similar in size and there is no predominant peak.

Examples of electrograms synthesized with minimal or no propagation disturbance imparted are shown in Figure 4B. The inset at left shows the configuration, with the diagonally oriented bipolar electrode being denoted as two solid circles, activation wavefronts shown as vertical lines, and propagation direction given by arrows. When a single rectilinear wavefront crosses a diagonally oriented bipolar electrode, the result is the top trace in panel B, a typical biphasic electrogram shape. The time instances 1 and 2 from the inset are shown along the model-generated electrogram. The biphasic amplitude of the deflection is 2 mV as noted by the scale at right. Similarly, when discontinuous rectilinear wavefronts pass the bipolar electrode at

different times, the result is a double potential (middle and lower trace in panel B). The middle trace in Figure 4B is based on two discontinuous wavefronts of equal length (the configuration is at left). The lower trace in Figure 4B is based on three discontinuous wavefronts – a long central wavefront and very short peripheral wavefronts (see configuration at left).

Examples of electrograms synthesized with a significant propagation disturbance imparted as a highly variable thin-to-thick LB transition are shown in Figure 4C. The largest peaks are of similar size and there is no predominant peak. There are also some broad deflections. The duration of the synthetic fractionation extends along much of the 175ms interval shown. In the bottom trace of panel C, peaks that extend above a threshold level and that would be separately counted as distinct peaks for quantitatively characterizing the degree of fractionation are noted by asterisks, with the average electrogram level as determined from spline interpolation being used as a reference for determining the height of the peaks in the normal direction, shown as a dashed line (see methodology). Based on the scale at right, the maximum change in electrogram amplitude is less than 1mV in amplitude.

Examples of actual fractionated electrograms acquired during normal sinus rhythm are shown in Figure 5A. These electrograms were acquired from LBs while the wavefront propagation direction was approximately parallel to the LB. Examples of electrograms synthesized when the activation wavefront travels in parallel to the LB are shown in Figure 5B. In these model-derived VT electrograms, based on the scale at right, individual deflections are less than 1mV in amplitude. The VT activation map corresponding to the traces of Figure 5A, and functional block line locations during this VT, is given on the left side in Figure 5C. The earliest activation is in red and latest is in blue color. A sinus rhythm activation map for this canine experiment is shown at right in Figure 5C. The locations of VT functional block are

overlaid on the sinus rhythm activation map as dotted lines. The recording sites from which the actual sinus rhythm electrograms of panel A were obtained are denoted by squares in the sinus rhythm activation map of panel C. The wavefront propagation direction during sinus rhythm, as shown by arrows, is in parallel with the LBs. The sinus rhythm electrograms of recording sites 44 and 45 were acquired from the location where the isthmus entrance would be present during VT, while the sinus rhythm electrogram of recording site 75 was acquired from the location where the isthmus exit would be present during VT.

In Figure 6 are shown IBZ activation maps with activation times from early (red) to late (blue). The activation map during monomorphic VT with double-loop reentrant circuit is shown in panel A. V-Pacing at the same cycle length is shown in panel B, with functional block forming around the stimulus site. Although there is some smoothing of the isochrones by the automated mapping program, at each line of block there is a difference of at least 40 milliseconds in the activation time on either side, and the wavefront curves around the sides of the block line as it propagates outward. In the V-pace map of panel B, the functional block lines tend to form near the edges of the isthmus boundary location. The overlap of the functional block lines forming during VT (panel A) and during V-Pacing (panel B) are shown in Figure 6C, with the lines forming during V-Pacing delineated in gray. The good coincidence in the overlap suggests that the location where functional block can form around the isthmus during reentrant VT can be detected by V-pacing from the isthmus area at a cycle length comparable to the VT cycle length.

In Figure 7, a monomorphic VT activation map is shown in panel A, and in panel B are drawn selected electrogram tracings recorded during sinus rhythm, and during the same monomorphic VT as is shown in panel A. Examples of electrogram recordings, from channels 71-80, are shown in panel B for both VT and sinus rhythm. Vertical bars mark the extend of

electrogram fractionation, when it occurs. Their locations on the electrode grid of panel A are marked by channel numbers from 71-80 for reference to the traces in panel B. Sites of fractionation during sinus rhythm (pink circles) and during VT (light blue circles) are shown in panel A. Electrogram fractionation is more widespread in VT as compared with sinus rhythm. During both sinus rhythm and during VT, many fractionated sites are adjacent to LBs, in accord with our fractionation model. However, fractionation is not present at all LB sites, and some sinus rhythm and VT fractionation sites do not overlap, as would be expected according to the model, since genesis of fractionation requires significant spatial variation in the thin-to-thick IBZ transition at the LBs, and it also depends on wavefront orientation with respect to the LBs.

Summary Statistics

For all experiments, 67.7% of VT functional block lines, as determined from activation mapping, were coincident with V-Pace functional block lines. In Table 1 are shown details of the overlap association for individual fractionated electrogram recording sites. The overlap of V-Pace versus VT fractionation sites was 77.3%, while the overlap of sinus rhythm fractionation sites with both VT and with V-Pace fractionation sites was about one third.

Electrogram fractionation site characteristics are noted in Table 1B. During reentrant VT for all experiments, there were an average of 18.8 ± 7.2 fractionated electrogram sites per 196 total sites (Table 1B). A mean of 15.2 ± 7.7 (80.9%) of those fractionated sites were adjacent to VT block line locations at the LBs. During sinus rhythm, there were an average of 14.8 ± 6.1 fractionated electrogram sites. A mean of 11.3 ± 6.8 (76.4%) of those sinus rhythm fractionated sites were adjacent to VT block line locations at the LBs. In the middle column, data for V-Pace is shown and it is intermediate to the results of VT and sinus rhythm. Overall, therefore, most recording sites where electrograms are fractionated are in proximity to the locations where

functional block lines form at the LBs.

The morphological characteristics for actual and model-derived fractionated electrograms are provided in Table 1C. The mean number of deflections, time between deflections, and number of zero-crossings appear to be similar for VT, V-Pace, and the perpendicular propagation model. The morphologic characteristics of sinus rhythm appear to be similar to the parallel propagation model values. Statistical comparisons of these numbers are provided in Table 1D. All possible comparisons are shown, with measurements that were expected to be similar noted without shading (only 3/12 of these comparisons showed a significant difference as noted by asterisks) and measurements expected to be dissimilar noted with gray shading (13/15 of these comparisons showed a significant difference). The respective values for sinus rhythm and the parallel propagation model are therefore mostly similar to each other and dissimilar to the values for VT, V-Pace and the perpendicular model. This suggests that wavefront propagation tends to be outward across the LBs during VT and V-Pace, but in parallel with the LBs during sinus rhythm, leading to differing statistical properties of fractionated electrograms during VT and V-Pace versus sinus rhythm.

The time between electrogram deflections pooled from all experiments was 9.24 ± 4.35 ms during sinus rhythm (Table 1C), which compared with a value of 12.19 ± 4.18 ms measured for a single experiment. During VT, the time between electrogram deflections pooled from all experiments was 16.32 ± 8.86 (Table 1C), as compared with a value of 16.15 ± 5.24 ms for a single experiment. For both sinus rhythm and VT, there were no significant differences between the means and standard deviations in pooled versus single experiment results ($p > 0.05$), thus suggesting that electrogram morphology is uncorrelated between recording sites.

Discussion

Summary

A model was developed to describe the genesis of local electrogram fractionation during reentrant VT and during sinus rhythm, and its dependency on activation wavefront orientation with respect to sharp transitions in IBZ thickness at the LBs. It was hypothesized that heterogeneity in the thin-to-thick transition at the LBs could cause activation wavefront curvature at each point to approach critical convexity with varying degree, so that propagation across these regions would be very slow and discontinuous according to the range of parameters given in Figure 1A. The wavefront discontinuity results from variability in $\Delta T/T$ and therefore in the convexity of wavefront curvature approaching the critical value. The statistical characteristics of VT and V-Pace fractionated electrograms have properties similar to model-derived fractionation with wavefront propagation perpendicular to the LB, suggesting that this orientation predominates in the genesis of VT fractionation, and V-Pace fractionation when the pace site is located within the isthmus region. The statistical characteristics of sinus rhythm fractionated electrograms have properties more similar to model-derived fractionation with wavefront propagation parallel to the LB, suggesting that this orientation may predominate during the genesis of sinus rhythm fractionation.

Competing Models of Electrogram Fractionation

Although this study suggests that wavefront curvature can generate discontinuous conduction which leads to electrogram fractionation, it does not prove that this is the actual mechanism, even for sites overlapping the LB. Other models of fractionation have been proposed, described for both ventricles and atria of animals as well as in clinical studies, which may be responsible for at least some of the fractionation observed in this study. One of the earliest models showed

that fractionated electrograms are present in canine IBZ in healed infarcts where there is wide separation of individual myocardial fibers, which can be distorted in orientation^{11,12}. Slow and inhomogeneous activation resulting in electrogram fractionation can be caused by convolution in the wavefront pathway, with individual deflections representing depolarization of a distinct myocyte bundle, and the reduction in fractionated electrogram amplitude resulting from the sparsity of viable muscle fibers¹¹. In an earlier study¹¹ as in the present study, electrogram fractionation was detected during sinus rhythm as well as during VT, although differences in fractionation criteria altered the measured fractionation interval. Fractionation can also be caused by wavefront discontinuities and alterations in propagation direction caused by presence of local fibrosis of sufficient density²². Electrical heterogeneity can play a role in the complexity of electrogram deflections, as suggested by a gradual increase in electrogram fractionation as electrogram voltage decreases²³. Systolic interval shortening after either drift or acceleration of a moving vortex can manifest as electrogram fractionation due to the change in source location²⁴. All of these other mechanisms are likely responsible for some electrogram fractionation observed in our current study, particularly for recording sites away from LB regions. Since these experiments were done in 3-5 day old canine infarction, it is unlikely that a finalized form of fibrosis played a major role in the genesis of the observed fractionation. In contrast, interstitial inflammation, swelling, and islands of electrophysiologically abnormal areas would be present. Although thinning and convolution of surviving strands of myocardial fibers can result in fractionation, this mechanism would likely only be valid for any fractionation observed within the isthmus location itself, where the IBZ is thinnest and thus the surviving strands are fewest. Furthermore, the findings of a recent clinical study suggest that fibrosis is not coincident with the location of fractionated atrial electrograms²⁵. Regardless of the mechanism which causes the

discontinuous conduction leading to fractionation, it is actually the lack of spatiotemporal resolution in the electrogram recordings that results in a fractionated electrogram appearance²⁶.

The New Fractionation Model

In several previous acute canine postinfarction studies which utilized magnetic resonance imaging and histologic analysis to determine the IBZ geometry, sharp and variable thin-to-thick transitions were shown to occur only at the LBs^{2,5,6}. Based on the new model, which was developed from this observation, fractionated electrograms form at IBZ locations where the parameters of Eq. 1 cause the slope of the trace in Figure 1A to be steep (noted with asterisk in Figure 1C). The steep region of the curve will be manifested at portions of the IBZ with smallest thickness T extending sharply to thicker regions, so that ΔT is large, and therefore $\Delta T/T$ is maximally large. Only at the LBs, where the thinnest border zone changes rapidly to thicker border zone, do these conditions occur. As we have shown elsewhere¹⁶ LBs are not necessarily oriented in the muscle fiber direction, and can even be perpendicular to this direction.

Point locations were used to define the leading edge of the activation wavefront. The multiple point sources caused a jagged electrogram shape because the distance between each source and the observation point changes by a discrete value during each time step. Whereas, when the activation wavefront leading edge is modeled as a continuous surface, the change in source location would not be as abrupt from one time step to the next, which would result in a more continuous electrogram shape. Likewise, the use of point electrodes in this study rather than electrodes with finite surface areas increased the jaggedness of the fractionated electrogram morphology, since passage of the wavefront across the electrode occurs more abruptly.

Our observations were made in canine hearts with coronary occlusion and may not be directly applicable to electrogram fractionation in all clinical cases of postinfarction VT. The

model is not representative of structural heterogeneities caused by fibrosis and tissue remodeling that can also be present in clinical postinfarction scars. The mathematical formulation used only represents changes in IBZ thickness and wavefront curvature. While thickness changes are present in scars causing clinical reentrant VT, other structural heterogeneities that alter the ratio of source current to load may also be present including tissue expansion, bifurcation, uncoupling of muscle fibers, and sharp wavefront curvature around unexcitable fibrotic scar tissue, which can result in similar effects to those we have attributed to the LBs. While the geometry of our model was therefore idealized, it nevertheless serves as an initial platform to estimate locations where fractionation can occur, and is in partial agreement with actual canine data (Table 1).

Our findings also suggest that quantitative analysis of sinus rhythm electrogram recordings can be useful in detecting arrhythmogenic regions, as is also possible using noncontact mapping data²⁷. However, fewer fractionated electrogram sites can be detected during sinus rhythm, due in part to the slower activation rate¹⁹ and because wavefront propagation may sometimes be oriented in the direction thick-to-thin across the LBs, which would not result in a discontinuous wavefront (Figure 1).

Conclusions

A model was developed which indicates that at transitions from thinnest to thicker IBZ, spatial variations in the geometry of the conducting medium cause localized differences in activation wavefront velocity, which can result in electrogram fractionation. Specifically, when $\Delta T/T < \sim 0.4$, which is most likely to occur at the LBs², convex wavefront curvature and very slow conduction can occur, which when variable cause discontinuous conduction and electrogram fractionation, with the amplitudes of the individual deflections being less than 1 mV (Figures 4 and 5). In part due to changes in wavefront orientation during sinus rhythm, and also because of

the rate-dependence of critical curvature¹⁹, very slow conduction and block are more likely during the shorter cycle lengths of reentrant VT, and during V-pacing when the stimulation site is within the reentry isthmus location. The activation wavefront can propagate in parallel to LBs during sinus rhythm, leading to fractionation which is of a shorter duration due to the more normal speed of the central portion of the wavefront (Figure 2C). We compared actual fractionation with model-generated fractionation based on a statistical analysis. Since thin-to-thick IBZ transitions are not necessarily oriented transverse to the muscle fiber axis^{2,16,28}, this model can account in part for the observation that functional block, with its associated fractionation, can occur off-axis to muscle fibers, or even transverse to muscle fibers¹⁶. The model can possibly be used to predict actual fractionated electrogram morphology that would be generated by a particular LB geometry, but would require evaluation of Eq. 2 without approximation, and knowledge of the precise orientation and geometry of each bipolar electrode as well as the wavefront leading edge at all time epochs.

Circulation
Arrhythmia and Electrophysiology
JOURNAL OF THE AMERICAN HEART ASSOCIATION

Limitations

For simplicity, wavefront propagation was considered to be constrained to travel in directions either perpendicular or parallel to LBs by our model. Propagation along an intermediate angle will likely result in intermediate fractionation properties. To reduce complexity we did not consider zigzag conduction, intramural conduction, or transmural conduction, the subject of future research. The number of experiments in which fractionation was measured in this study, 10, is limited. Confirmation with a larger pool of experiments should be done.

Acknowledgments: Dr. Nicholas S. Peters acknowledges funding from the British Heart Foundation (RG/10/11/28457 and Centre of Research Excellence), and the NIHR Biomedical Research Centre.

Conflict of Interest Disclosures: None.

References:

1. Stevenson WG. Ventricular scars and ventricular tachycardia. *Trans Am Clin Climatol Assoc.* 2009;120:403-412.
2. Ciaccio EJ, Ashikaga H, Kaba RA, Cervantes D, Hopenfeld B, Wit AL, Peters NS, McVeigh ER, Garan H, Coromilas J. Model of reentrant ventricular tachycardia based on infarct border zone geometry predicts reentrant circuit features as determined by activation mapping. *Heart Rhythm.* 2007;4:1034-1045.
3. Ashikaga H, Sasano T, Dong J, Zviman MM, Evers R, Hopenfeld B, Castro V, Helm RH, Dickfeld T, Nazarian S, Donahue JK, Berger RD, Calkins H, Abraham MR, Marbán E, Lardo AC, McVeigh ER, Halperin HR. Magnetic resonance-based anatomical analysis of scar-related ventricular tachycardia: implications for catheter ablation. *Circ Res.* 2007;101:939-947.
4. Ciaccio EJ. Characteristics of critical isthmus sites during reentrant ventricular tachycardia. *Heart Rhythm.* 2011;8:1950-1951.
5. Wit AL, Allesie MA, Bonke FI, Lammers W, Smeets J, Fenoglio JJ Jr. Electrophysiologic mapping to determine the mechanism of experimental ventricular tachycardia initiated by premature impulses. *Am J Cardiol.* 1982;49:166-185.
6. Peters NS, Coromilas J, Severs NJ, Wit AL. Disturbed connexin43 gap junction distribution correlates with the location of reentrant circuits in the epicardial border zone of healing canine infarcts that cause ventricular tachycardia. *Circulation.* 1997;95:988-996.
7. Ashikaga H, Mickelsen SR, Ennis DB, Rodriguez I, Kellman P, Wen H, McVeigh ER. Electromechanical analysis of infarct border zone in chronic myocardial infarction. *Am J Physiol Heart Circ Physiol.* 2005;289:H1099-H1105.
8. Kocovic DZ, Harada T, Friedman PL, Stevenson WG. Characteristics of electrograms recorded at reentry circuit sites and bystanders during ventricular tachycardia after myocardial infarction. *J Am Coll Cardiol.* 1999;34:381-388.
9. Aliot EM, Stevenson WG, Almendral-Garrote JM, Bogun F, Calkins CH, Delacretaz E, Della Bella P, Hindricks G, Jaïs P, Josephson ME, Kautzner J, Kay GN, Kuck KH, Lerman BB, Marchlinski F, Reddy V, Schalij MJ, Schilling R, Soejima K, Wilber D; European Heart Rhythm Association (EHRA); Registered Branch of the European Society of Cardiology (ESC); Heart Rhythm Society (HRS); American College of Cardiology (ACC); American Heart Association (AHA). EHRA/HRS Expert Consensus on Catheter Ablation of Ventricular Arrhythmias: developed in a partnership with the European Heart Rhythm Association (EHRA), a Registered Branch of the European Society of Cardiology (ESC), and the Heart Rhythm Society (HRS); in collaboration with the American College of Cardiology (ACC) and the American Heart Association (AHA). *Heart Rhythm.* 2009;6:886-933.

10. Kienzle MG, Miller J, Falcone RA, Harken A, Josephson ME. Intraoperative endocardial mapping during sinus rhythm: relationship to site of origin of ventricular tachycardia. *Circulation*. 1984;70:957-965.
11. Gardner PI, Ursell PC, Fenoglio JJ Jr, Wit AL. Electrophysiologic and anatomic basis for fractionated electrograms recorded from healed myocardial infarcts. *Circulation*. 1985;72:596-611.
12. Ursell PC, Gardner PI, Albala A, Fenoglio JJ Jr, Wit AL. Structural and electrophysiological changes in the epicardial border zone of canine myocardial infarcts during infarct healing. *Circ Res*. 1985;56:436-451.
13. Dillon SM, Allessie MA, Ursell PC, Wit AL. Influences of anisotropic tissue structure on reentrant circuits in the epicardial border zone of subacute canine infarcts. *Circ Res*. 1988;63:182-206.
14. Ciaccio EJ, Saltman AE, Hernandez OM, Bornholdt RJ, Coromilas J. Multichannel data acquisition system for mapping the electrical activity of the heart. *Pacing Clin Electrophysiol*. 2005;28:826-838.
15. Hopenfeld B, Ashikaga H, McVeigh ER. Geodesic based registration of sensor data and anatomical surface image data. *Ann Biomed Eng*. 2007;35:1771-1781.
16. Ciaccio EJ, Costeas C, Coromilas J, Wit AL. Static relationship of cycle length to reentrant circuit geometry. *Circulation*. 2001;104:1946-1951.
17. Cabo C, Pertsov AM, Baxter WT, Davidenko JM, Gray RA, Jalife J. Wave-front curvature as a cause of slow conduction and block in isolated cardiac muscle. *Circ Res*. 1994;75:1014-1028.
18. Clayton RH, Holden AV. Computational framework for simulating the mechanisms and ECG of re-entrant ventricular fibrillation. *Physiol Meas*. 2002;23:707-726.
19. Jadidi AS, Duncan E, Miyazaki S, Lellouche N, Shah AJ, Forclaz A, Nault I, Wright M, Rivard L, Liu X, Scherr D, Wilton SB, Sacher F, Derval N, Knecht S, Kim SJ, Hocini M, Narayan S, Haïssaguerre M, Jaïs P. Functional nature of electrogram fractionation demonstrated by left atrial high-density mapping. *Circ Arrhythm Electrophysiol*. 2012;5:32-42.
20. Spach MS, Miller WT 3rd, Miller-Jones E, Warren RB, Barr RC. Extracellular potentials related to intracellular action potentials during impulse conduction in anisotropic canine cardiac muscle. *Circ Res*. 1979;45:188-204.
21. Ciaccio EJ, Dunn SM, Akay M, Wit AL, Coromilas J, Costeas CA. Localized spatial discrimination of epicardial conduction paths after linear transformation of variant information. *Ann Biomed Eng*. 1994;22:480-492.
22. Jacquemet V, Henriquez CS. Genesis of complex fractionated atrial electrograms in zones of

- slow conduction: a computer model of microfibrosis. *Heart Rhythm*. 2009;6:803-810.
23. Liuba I, Walfridsson H. Focal atrial tachycardia: increased electrogram fractionation in the vicinity of the earliest activation site. *Europace*. 2008;10:1195-1204.
24. Atienza F, Calvo D, Almendral J, Zlochiver S, Grzeda KR, Martínez-Alzamora N, González-Torrecilla E, Arenal A, Fernández-Avilés F, Berenfeld O. Mechanisms of fractionated electrograms formation in the posterior left atrium during paroxysmal atrial fibrillation in humans. *J Am Coll Cardiol*. 2011;57:1081-1092.
25. Jadidi AS, Cochet H, Shah AJ, Kim SJ, Duncan E, Miyazaki S, Sermesant M, Lehrmann H, Lederlin M, Linton N, Forclaz A, Nault I, Rivard L, Wright M, Liu X, Scherr D, Wilton SB, Roten L, Pascale P, Derval N, Sacher F, Knecht S, Keyl C, Hocini M, Montaudon M, Laurent F, Haïssaguerre M, Jaïs P. Inverse relationship between fractionated electrograms and atrial fibrosis in persistent atrial fibrillation: combined magnetic resonance imaging and high-density mapping. *J Am Coll Cardiol*. 2013;62:802-812.
26. Correa de Sa DD, Thompson N, Stinnett-Donnelly J, Znojkwicz P, Habel N, Müller JG, Bates JH, Buzas JS, Spector PS. Electrogram fractionation: the relationship between spatiotemporal variation of tissue excitation and electrode spatial resolution. *Circ Arrhythm Electrophysiol*. 2011;4:909-916.
27. Ciaccio EJ, Chow AW, Kaba RA, Davies DW, Segal OR, Peters NS. Detection of the diastolic pathway, circuit morphology, and inducibility of human postinfarction ventricular tachycardia from mapping in sinus rhythm. *Heart Rhythm* 2008;5:981-991.
28. Ciaccio EJ. Ablation targets in reentrant ventricular tachycardia. *Heart Rhythm*. 2013;10:1117-1118.

Table 1A: Fractionation Recording Site Association

Description	Overlap
VT/VP Fractionation	77.3%
VT/SR Fractionation	31.3%
VP/SR Fractionation	34.4%

VT = reentrant ventricular tachycardia, VP = ventricular pacing during sinus rhythm, SR = normal sinus rhythm.

Table 1B: Fractionated Site Characteristics

Description	VT	VP	SR
Fractionated Electrogram Sites	18.8 ± 7.2	15.7 ± 9.8	14.8 ± 6.1
Frac Sites associated with LB	15.2 ± 7.7 (80.9%)	12.6 ± 8.9 (80.3%)	11.3 ± 6.8 (76.4%)

VT = reentrant ventricular tachycardia, VP = ventricular pacing during sinus rhythm, SR = normal sinus rhythm. Frac = fractionated electrogram, LB = lateral boundary.

JOURNAL OF THE AMERICAN HEART ASSOCIATION

Table 1C: Morphological Characteristics of Fractionated Electrograms

Fractionation Type	# of Deflections	Time between Deflections (ms)	# Zero-Crossings
Perpendicular Model Frac	9.44 ± 2.39	14.36 ± 5.17	25.15 ± 2.42
VT	7.60 ± 1.18	16.32 ± 8.86	19.56 ± 5.48
VP	7.26 ± 1.43	14.40 ± 4.81	21.15 ± 6.69
Parallel Model Frac	6.73 ± 3.10	7.10 ± 3.75	11.30 ± 2.53
SR	5.85 ± 1.77	9.24 ± 4.35	10.50 ± 2.48

VT = reentrant ventricular tachycardia, VP = ventricular pacing during sinus rhythm, SR = normal sinus rhythm, Frac = fractionated electrogram, btwn = between, ms = milliseconds, # = number of.

Table 1D: Statistical Characteristics of Fractionated Electrograms

TOP			
Fractionation Type	# of Deflections	Time between Deflections (ms)	# Zero-Crossings
VT – Perpendicular Model	P = 0.0038*	P = 0.3982	P = 0.0002*
VP – Perpendicular Model	P = 0.0012*	P = 0.9799	P = 0.0163
SR – Parallel Model	P = 0.2772	P = 0.1039	P = 0.3190
VT to VP	P = 0.4173	P = 0.3997	P = 0.4161
BOTTOM			
VT – Parallel Model	P = 0.2481	P = 0.0001*	P < 0.0001*
VP – Parallel Model	P = 0.4917	P < 0.0001*	P < 0.0001*
SR – Perpendicular Model	P < 0.0001*	P = 0.0016*	P < 0.0001*
VT to SR	P = 0.0007*	P = 0.0027*	P < 0.0001*
VP to SR	P = 0.0086*	P = 0.0010*	P < 0.0001*

* = significance ($p < 0.01$), VT = reentrant ventricular tachycardia, VP = ventricular pacing during sinus rhythm, SR = normal sinus rhythm, btwn = between, ms = milliseconds, # = number of. N = 20 for each group. Measurements expected to be similar, so that no significant differences would be anticipated to occur, are shown in TOP panel. Measurements expected to be dissimilar, with the expectation of significant difference, are shown in BOTTOM panel.

Figure Legends:

Figure 1: Relationship between time for propagation across a 1 millimeter distance and activation wavefront curvature in the infarct border zone. The ordinate axis shows the time to travel a 1mm distance and the abscissa is the right-hand term in Eq. 1. The right-hand-term is shown ranging from 0 (rectilinear wavefront) to 0.39. In panel A the right-hand term is noted

with negative sign (convex wavefront curvature causing deceleration), in panel B it is noted for positive sign (concave wavefront curvature causing acceleration), and in panel C both are graphed for comparison.

Figure 2: The relationship between infarct border zone thickness and wavefront propagation. A. The infarct is given by the solid green region. The infarct border zone is considered to be above the infarct and is bounded above by the epicardial surface. Wavefront propagation direction during reentrant ventricular tachycardia is denoted by arrows. The red surfaces denote the degree of wavefront curvature – it is concave along the Z-axis direction at the isthmus entrance at left, rectilinear within the isthmus region at center, and convex along the Z-axis direction at the isthmus exit at right. There is a sharp thin-to-thick transition in infarct border zone depth away from the LBs, which prevents outward propagation there. B. The same basic model; however now the thin-to-thick transition at the LBs is more gradual and it is also variable. Slow outward conduction can occur, with the conduction velocity depending upon the sharpness of the spatial change in depth of infarct border zone (short arrows). C. The model of panel B observed from above. During sinus rhythm, wavefront propagation can occur in the direction shown, which is in parallel with the lateral boundaries. When a portion of the wavefront encounters a sharp thin-to-thick transition, block occurs as noted by short black lines. The wavefront must then propagate around the block line.

Figure 3: The schematic representation of the set-up used for generating virtual electrograms. A. Configuration for calculating the extracellular potential for a sheet of cardiac muscle. The discrete spatial intervals used for calculation are dx dy , which are each 1 millimeter in this study.

For Eq. 6, it was supposed that $b = 0$ and $a \ll d$. B. The configuration of the wavefront leading edge after transition across a thin-thick boundary, and the diagonally oriented bipolar electrode.

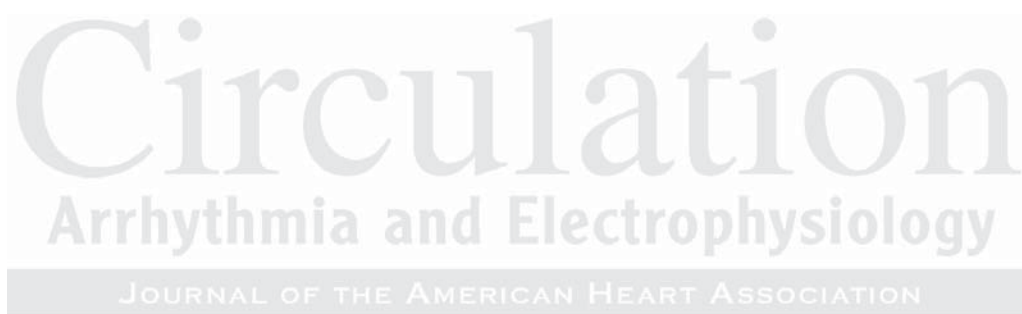
Figure 4: Examples of actual fractionated electrograms recorded during reentrant ventricular tachycardia (A), synthesized electrograms with minimal or no propagation disturbance (B), and synthesized fractionated electrograms with significant propagation disturbance across the lateral boundary (C). The duration of all traces in Figure 3 is 175ms, as shown by the scale at top. In the inset to the left of the traces in panel B, the bipolar electrode orientation is depicted using solid circles, and wavefronts at two time instances 1 and 2 are denoted by straight lines.

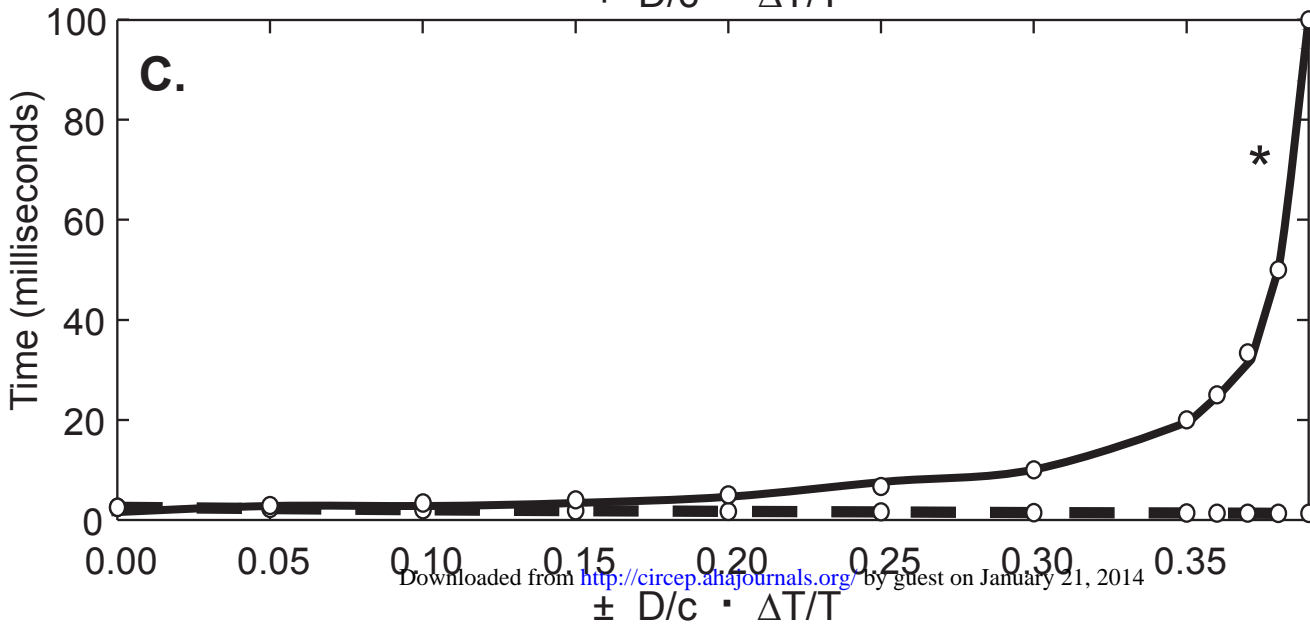
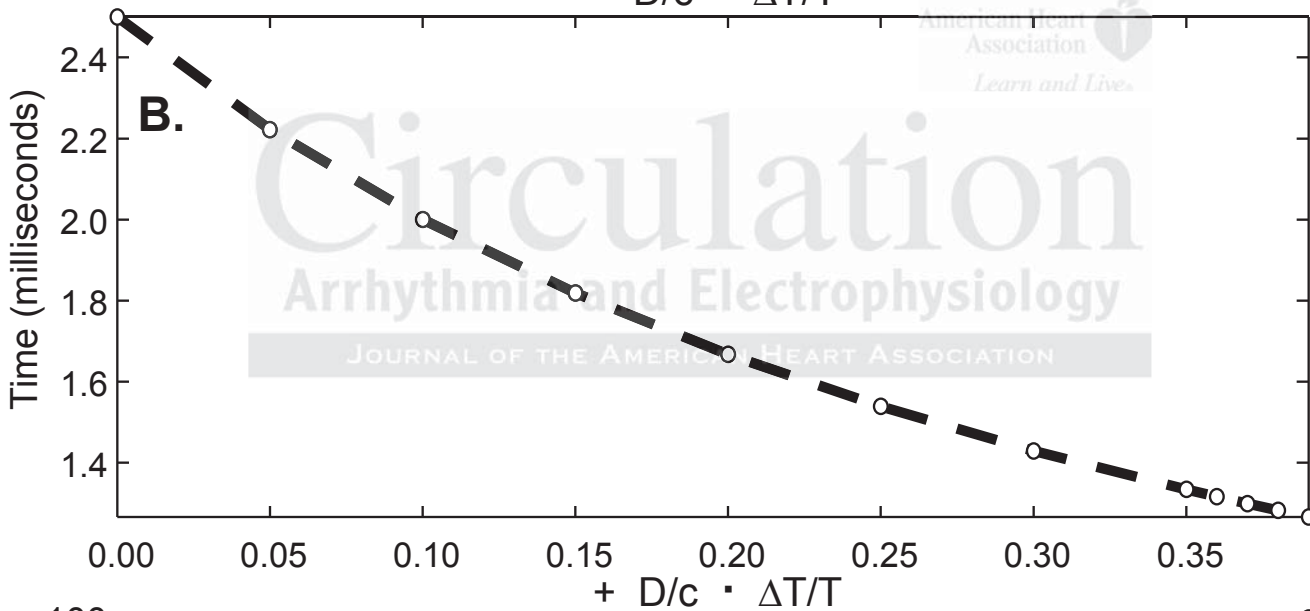
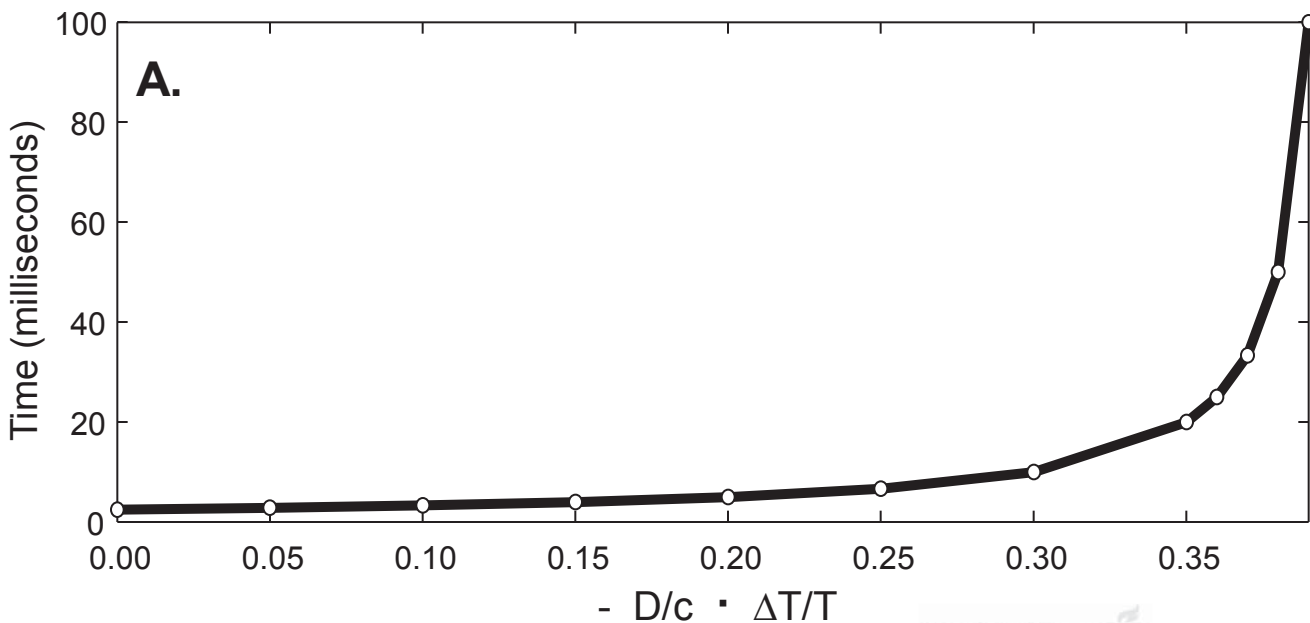
Figure 5: Examples of actual fractionated electrograms acquired during normal sinus rhythm from the infarct border zone (A), and synthesized fractionated electrograms when the activation wavefront propagates in parallel with a thickness transition boundary (B) with activation maps showing recording site locations (C).

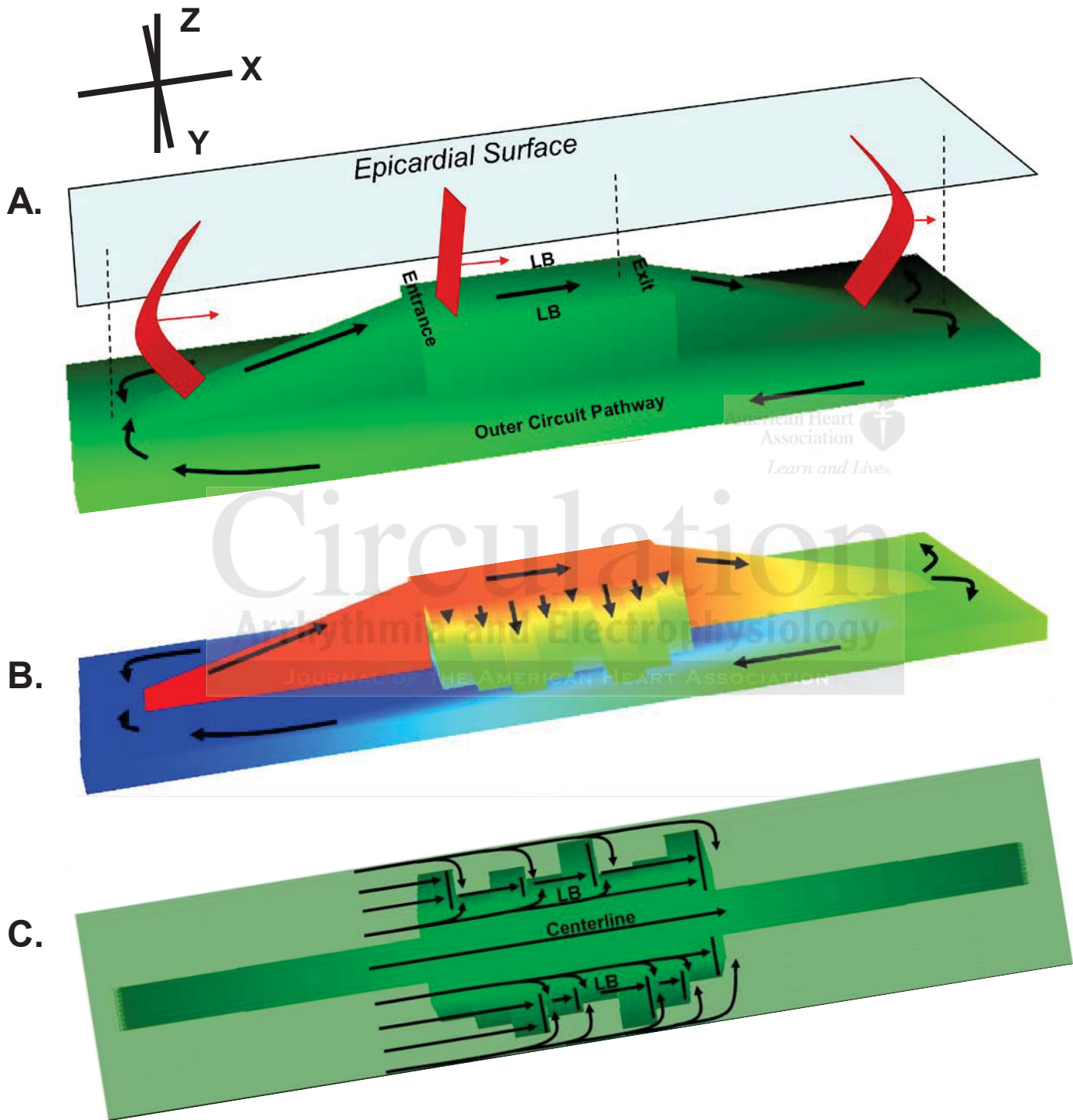
Figure 6: Activation map showing the relationship between functional conduction block during reentrant ventricular tachycardia occurring in the epicardial border zone (A) and V-pace in the same experiment (B). The V-Pace stimulation site is marked. Earliest activation is shown in red and the latest is in blue color. Areas of very slow conduction or functional block are delineated with thick curved black lines. The overlap of functional block line locations from panels A and B is shown in panel C.

Figure 7: A reentrant VT activation map is shown at top, with the location of functional block

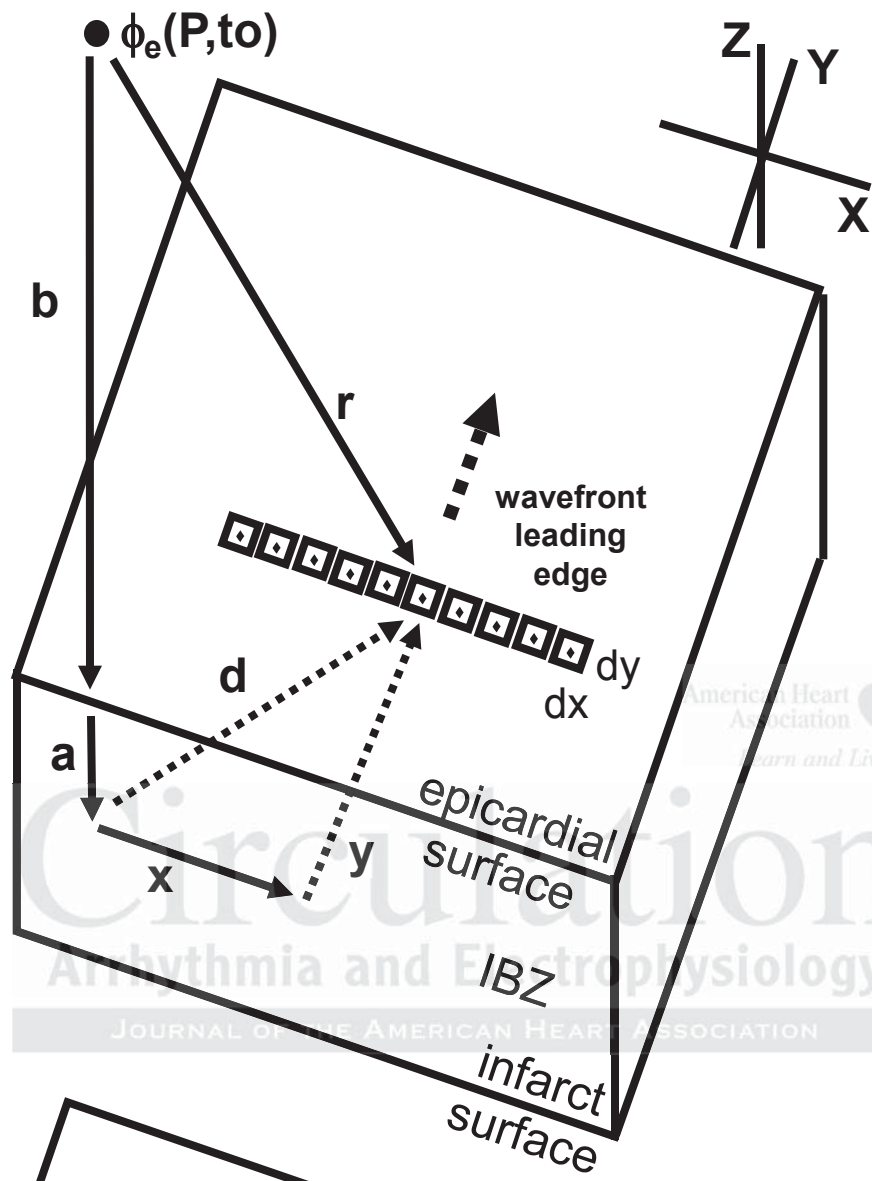
lines being denoted by curved black lines. The earliest activation is in red and latest is in blue color as in Figures 5 and 6. Isochrones and activation times at individual recording sites are noted, and arrows show the direction of wavefront propagation during reentrant ventricular tachycardia. The locations of fractionated electrogram sites for those recordings acquired during ventricular tachycardia are marked with light blue circles and for sinus rhythm the sites are noted by pink circles. Examples of fractionated electrogram recordings from this experiment are shown in panel B for sinus rhythm and ventricular tachycardia.



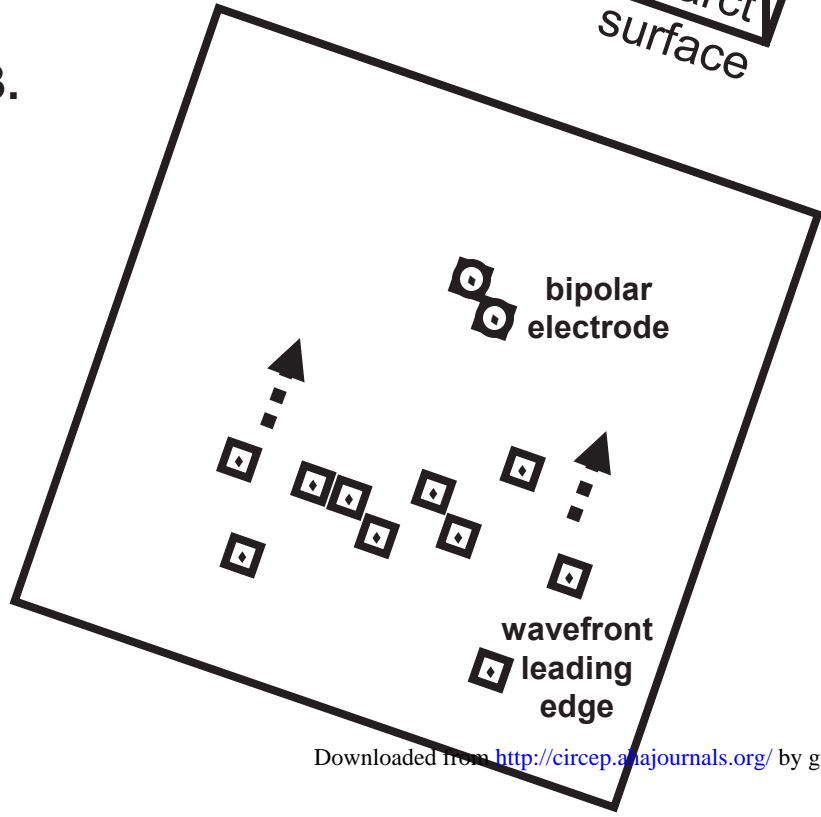




A.



B.



American Heart Association
Learn and Live.
Circulation
Arrhythmia and Electrophysiology
JOURNAL OF THE AMERICAN HEART ASSOCIATION

